


Soliton collisions in Bose-Einstein condensates with current-dependent interactionsQian Jia  and Haibo Qiu *School of Science, Xi'an University of Posts and Telecommunications, Xi'an 710121, China*Antonio Muñoz Mateo *Departamento de Física, Universidad de La Laguna, La Laguna, Tenerife 38200, Spain*

(Received 26 August 2022; accepted 18 November 2022; published 19 December 2022)

We study general collisions between chiral solitons in Bose-Einstein condensates subject to combined attractive and current-dependent interatomic interactions. A simple analysis based on the linear superposition of the solitons allows us to determine the relevant time and space scales of the dynamics, which is illustrated by extensive numerical simulations. By varying the differential amplitude, the relative phase, the average velocity, and the relative velocity of the solitons, we characterize the different dynamical regimes that give rise to oscillatory and interference phenomena. Apart from the known inelastic character of the collisions, we show that the chiral dynamics involves an amplitude reduction with respect to the case of regular solitons. To compare these results with feasible ultracold-gas experiments, the influence of harmonic confinement is analyzed in both the emergence and the interaction of chiral solitons.

DOI: [10.1103/PhysRevA.106.063314](https://doi.org/10.1103/PhysRevA.106.063314)**I. INTRODUCTION**

Research on matter-wave solitons has entered a new stage since the first experiments on collapsing Bose-Einstein condensates (BECs) of ultracold gases [1,2]. The whole process of emergence and evolution of bright solitons could be observed in experiments that, by making use of magnetic Feshbach resonances of some atomic species, tuned the interatomic forces from repulsive to attractive interactions [3,4]. In this way, stable bright matter solitons were generated in elongated condensates with quasi-one-dimensional (quasi-1D) geometries; in most of the cases, an external harmonic potential is necessary to keep the atomic cloud trapped [5].

The realization of matter-soliton trains led naturally to the study of soliton collisions [4,6,7]. This scenario allowed for the experimental testing in ultracold gases of predictions that had been made long before for bright soliton interactions in optical fibers [8,9]. In parallel, theoretical studies on matter solitons followed the experimental developments [10–15]. Currently, the interaction between bright solitons in the framework of the 1D nonlinear Schrödinger equation is reasonably well understood as a nonlinear-wave interference process during which Josephson tunneling of particles can take place [16,17]. However, there are still open, long-standing questions regarding the process of soliton generation and subsequent evolution that need detailed analysis in order to be settled. To this end, recent experiments that use nondestructive imaging have been carried out in scalar condensates [18,19].

This year, a new type of matter-wave soliton that shows chiral properties has been observed in experiments with ultracold atoms [20]. It was theoretically predicted in 1996 [21], and its existence relies on the action of a density-dependent gauge field, which provides the system with chiral properties. The experimental realization of density-dependent gauge

fields in ultracold atoms had been achieved in the presence of optical lattices [22,23], but only very recently has it been realized in translational-invariant settings [20,24]. The emergent chiral properties of the system are reflected also in the free expansion of the atomic cloud and the onset of persistent currents [25], or the center of mass oscillations [26], and are particularly manifest in the direction-dependent motion (and existence) of bright, chiral solitons [20,21,27].

Before the experiments described in Ref. [20] took place, chiral solitons had been demonstrated to be dynamically stable objects [28]. The collisions between chiral solitons with an equal number of particles had been studied [29], where a nonintegrable dynamics stands out as the main difference with respect to the collisions of regular solitons. The action of the modulational instability has also been analyzed in the presence of a density-dependent gauge field and in the absence of trapping [30], showing the chiral features of the resulting soliton train. Still, as can be inferred from a comparison with the extensive literature on regular solitons, the study of chiral solitons is just starting and requires further characterization, the more so with the prospect of experimental testing.

This paper contributes to this characterization by analyzing general collisions between chiral solitons with different numbers of particles, including the variation of both the relative phase and the relative velocity. The collisions are studied first in the absence of confinement and later, motivated by the usual experimental settings, within a harmonic trap. The soliton emergence is also addressed in order to show the influence of the harmonic confinement. We characterize the dynamical regimes of chiral-soliton collisions, which are dominated by oscillatory and interference phenomena. The relative phase plays a more decisive role than in regular solitons, since it can determine the transmission and reflection coefficients of the

soliton scattering. Our analysis is made in the framework of a generalized Gross-Pitaevskii (GP) equation that, besides the usual contact-interaction term, includes a current-dependent interaction as derived from a nonlocal unitary transformation of the theory containing the density-dependent gauge field [21].

The rest of this paper is structured as follows: Sec. II provides a detailed introduction of the system model including the properties of relevant states, such as plane waves and solitons, trapped and untrapped, and their connection through dynamical decay. Section III presents the theoretical basis that rules the soliton collisions and their dynamical regimes, which are tested first for regular solitons and later for chiral solitons. Section IV summarizes our results. In Appendixes A and B we clarify the particular units employed in our analysis and provide additional details on several aspects of chiral-soliton collisions, respectively.

II. MODEL

We assume that the system is an elongated BEC at zero temperature with frozen transverse degrees of freedom, such that the order parameter of the three-dimensional (3D) condensate is space separable $\Psi(\mathbf{r}, t) = \psi(x, t)\chi(y, z)$, where $\chi(y, z)$ is the transverse ground state. We further assume, within a mean-field framework, that the axial wave function $\psi(x, t)$ follows a generalized 1D Gross-Pitaevskii equation

$$i\hbar \frac{\partial \psi}{\partial t} = \left[-\frac{\hbar^2}{2m} \frac{\partial^2}{\partial x^2} + U_{\text{ext}}(x) + g_{1\text{D}}|\psi|^2 + \hbar\kappa J \right] \psi, \quad (1)$$

where $U_{\text{ext}}(x)$ is an external axial potential, $g_{1\text{D}} < 0$ is the strength of the usual contact interparticle interaction, and $J(x, t)$ is the current density $J = \hbar(\psi^* \partial_x \psi - \psi \partial_x \psi^*) / (i2m)$. The latter quantity, which introduces a current-dependent mean field, can be demonstrated to enter the equation of motion, in a different representation (see Ref. [21] for details), through a density-dependent gauge field that induces a momentum shift of value $\hbar\kappa|\psi|^2/2$, where κ is the dimensionless strength of the gauge field.

After multiplication on the left of Eq. (1) by ψ^* , and subtracting the resulting equation from its complex conjugate, one obtains the continuity equation

$$\frac{\partial}{\partial t} |\psi|^2 + \frac{\partial}{\partial x} J = 0, \quad (2)$$

which, from the integration over the whole space $d/dt \int dx |\psi|^2 = 0$, gives the conservation of the number of particles $N = \int dx |\psi|^2$. Additionally, the Hamiltonian operator in Eq. (1), $H_{\text{GP}} = \hat{p}^2/2m + U_{\text{ext}} + g_{1\text{D}}|\psi|^2 + \hbar\kappa J$, endows the system with unusual global properties. The expectation value of the momentum operator $\langle \hat{p} \rangle = -i\hbar \int dx \psi^* \partial_x \psi$, which follows the generic equation $i\hbar d/dt \langle \hat{p} \rangle = \langle [\hat{p}, H_{\text{GP}}] \rangle$, gives, making use of the continuity equation,

$$\frac{d}{dt} \left\langle \hat{p} - \frac{\hbar\kappa}{2} |\psi|^2 \right\rangle = \left\langle -\frac{\partial U_{\text{ext}}}{\partial x} \right\rangle. \quad (3)$$

In the absence of external potential, the total mechanical momentum $\Pi = \int dx \psi^* (\hat{p} - \hbar\kappa|\psi|^2/2) \psi$ is conserved.

Analogously, the expectation value of the Hamiltonian, which follows an equation for a time-dependent operator, gives $d/dt \langle H_{\text{GP}} \rangle = \langle \partial_t (g_{1\text{D}}|\psi|^2 + \hbar\kappa J) \rangle$, and by using again the continuity equation, $d/dt \langle H_{\text{GP}} \rangle = d/dt \langle (g_{1\text{D}}|\psi|^2/2 + \hbar\kappa J) \rangle$, that is,

$$\frac{d}{dt} \int dx \psi^* \left(-\frac{\hbar^2}{2m} \frac{\partial^2}{\partial x^2} + U_{\text{ext}} + \frac{g_{1\text{D}}}{2} |\psi|^2 \right) \psi = 0; \quad (4)$$

so the total energy E given by the above, explicit κ -independent integral is a conserved quantity [21].

It is insightful to rewrite the current density as $J = |\psi|^2 v$, where the superfluid velocity $v(x, t) = \hbar \partial_x S / m$ is defined from the wave function phase $S(x, t) = \arg \psi$; hence Eq. (1) can be recast as

$$i\hbar \frac{\partial \psi}{\partial t} = \left[-\frac{\hbar^2}{2m} \frac{\partial^2}{\partial x^2} + U_{\text{ext}} + g_v |\psi|^2 \right] \psi, \quad (5)$$

where the velocity-dependent effective interaction g_v is defined by

$$g_v(x, t) = g_{1\text{D}} + \hbar\kappa v(x, t). \quad (6)$$

Therefore the effective interparticle interaction g_v changes its character (hence its sign) from attractive to repulsive when the local velocity exceeds the limit value set by the contact interaction $v > (v_g \equiv |g_{1\text{D}}/\hbar\kappa|)$; otherwise the effective interaction remains attractive for $v < v_g$.

The stationary states present the space-time separable wave function $\psi(x, t) = \psi(x) \exp(-i\mu t/\hbar)$, where μ is the eigenvalue of the Hamiltonian operator $H_{\text{GP}}\psi = \mu\psi$, but differently from the regular Gross-Pitaevskii equation, μ is not (in general) the chemical potential $\mu_{\text{ch}} = \partial_N E$. The spectrum of linear excitations $\delta\psi_j = [u_j, v_j]^T$ of stationary states, so that $\psi(x, t) \rightarrow \exp(-i\mu t/\hbar) \{ \psi(x) + \sum_j [u_j(x) \exp(-i\omega_j t) + v_j(x)^* \exp(i\omega_j^* t)] \}$, with j being a mode index, can be obtained through the Bogoliubov equations $B\delta\psi_j = \hbar\omega_j \delta\psi_j$, where the Bogoliubov matrix can be written as $B = B_{\text{GP}} + B_\kappa$, explicitly,

$$B_{\text{GP}} = \begin{pmatrix} H_{\text{GP}} + g_{1\text{D}}|\psi|^2 - \mu & g_{1\text{D}}\psi^2 \\ -g_{1\text{D}}\psi^{*2} & -H_{\text{GP}} - g_{1\text{D}}|\psi|^2 + \mu \end{pmatrix} \quad (7)$$

and

$$B_\kappa = i \frac{\hbar^2 \kappa}{2m} \begin{pmatrix} \psi \partial_x \psi^* - |\psi|^2 \partial_x & -\psi \partial_x \psi + \psi^2 \partial_x \\ -\psi^* \partial_x \psi^* + \psi^{*2} \partial_x & \psi^* \partial_x \psi - |\psi|^2 \partial_x \end{pmatrix}. \quad (8)$$

The existence of complex frequencies in the spectrum of linear excitations, that is, $\text{Im}(\omega_j) \neq 0$, indicates the presence of unstable modes that have an exponential growth (in the linear regime) from perturbative values, thus capable of breaking the stationary configuration.

A. Plane waves

For $U_{\text{ext}} = 0$, Eq. (1) is translational invariant; in this case, it is useful to look at the spectrum of plane-wave eigenstates $\psi_q(x, t) = \sqrt{n} \exp[i(qx - \mu_q t/\hbar)]$, having shifted frequencies $\omega_q = \mu_q/\hbar$ defined by

$$\mu_q = \hbar^2 q^2 / 2m + (g_{1\text{D}} + \hbar^2 \kappa q / m) n. \quad (9)$$

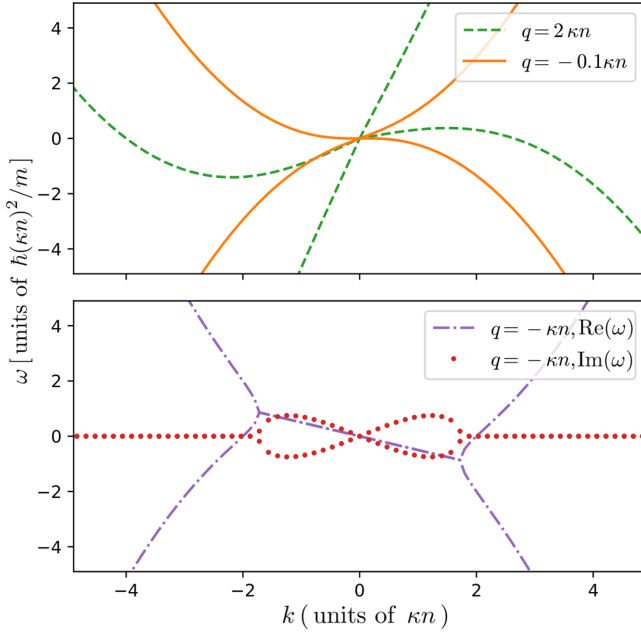


FIG. 1. Linear excitation frequencies ω of plane-wave states with wave number q in a system with current-dependent interactions (and $U_{\text{ext}} = 0$, $g_{1D} = 0$). For $q > -\kappa n/4$ (top panel) the plane-wave states are dynamically stable (all the excitation modes present real frequencies), and the speed of sound, $c_{\pm}^{\pm} = \partial_k \omega|_{k \rightarrow 0}$, is different for rightward and leftward moving waves [see Eq. (11)]. For $q < -\kappa n/4$ the plane-wave states are unstable against long-wavelength perturbation modes (bottom panel), which have imaginary frequencies.

Therefore the group velocity of the waves $v_q = \partial_q \mu_q / \hbar = \hbar(q + \kappa n)/m$ does not match the superfluid velocity $v = \hbar q/m$. As relevant for the generation of chiral solitons, we review the stability of plane-wave states, which has been recently analyzed in Ref. [30]. In addition, we will report on the related problem, usual in ultracold-gas experiments, of the instability of a smooth density profile in a harmonic trap.

The linear excitations of a plane wave ψ_q can also be expanded in Fourier modes $\delta\psi_k = e^{ikx} \{u \exp(iqx), v \exp(-iqx)\}^T$ that produce independent, algebraic Bogoliubov equations for each excitation mode with wave vector k . The resulting excitation dispersion is

$$\omega_{k\pm} = \frac{\hbar k}{m} \left(q + \frac{\kappa n}{2} \pm \sqrt{\frac{k^2 + (\kappa n)^2}{4} + q\kappa n + \frac{m g_{1D} n}{\hbar^2}} \right), \quad (10)$$

which is asymmetric, $|\omega_{k+}| \neq |\omega_{k-}|$ (see the top panel of Fig. 1), even as looked at from a moving frame with velocity $\hbar q/m$, and only becomes symmetric if looked at from a reference frame moving with velocity $\hbar(q + \kappa n/2)/m$. This fact reflects the origin of the current-density term in the generalized GP equation (1), which involves a momentum shift of $\hbar\kappa n/2$ due to the action of a density-dependent gauge field [21]. From the dispersion equation (10), the speed of sound $c_{\pm} = \partial_k \omega_{k\pm}$ is obtained for long-wavelength excitations

$k \rightarrow 0$ as

$$c_{\pm} = \frac{\hbar}{m} \left(q + \frac{\kappa n}{2} \pm \sqrt{\frac{(\kappa n)^2}{4} + q\kappa n + \frac{m g_{1D} n}{\hbar^2}} \right), \quad (11)$$

which also shows the chiral features of the system. As follows from Eq. (10), plane waves with wave vector $q < -[\kappa n/4 + m g_{1D}/(\hbar^2 \kappa)]$ are unstable against perturbations [30]. The bottom panel of Fig. 1 shows an example with $g_{1D} = 0$ and $q = -\kappa n$; in this case, all wave vectors below $-\kappa n/4$ correspond to unstable states. Intuitively, the origin of this modulation instability at $g_{1D} = 0$, when the system energy does not include any contribution from interparticle interactions, involves the conversion of local canonical momentum into local density by means of Eq. (3). Interestingly, in contrast to the case of just attractive interactions ($\kappa = 0$), it is possible to find dynamically stable states with negative effective interaction $g_v = \hbar^2 \kappa q/m < 0$ in the range $q \in [-\kappa n/4 + m g_{1D}/(\hbar^2 \kappa), 0]$. In particular, for $g_{1D} = 0$, the set of states with wave vectors $q \in [-\kappa n/4, 0]$ are dynamically stable. From inspection of Eq. (10), one can see that the cause of this extra stability resides in the zero-point energy $(\hbar\kappa n)^2/4m$ associated with moving excitation modes. In finite systems, due to the discrete spectrum, the stability window is enlarged by approximately $(2\pi/L)^2/(4\kappa n)$, where L is the system size, within the domain of negative wave numbers.

The dynamical decay of unstable plane waves gives rise to the segmentation of the initial constant density into localized, moving wave packets, akin to bright solitons, that interact with each other [30]. This process has been observed in BECs with attractive contact interactions [5], where the resulting number of solitons can be approximated by the ratio L/λ_{max} , where $\lambda_{\text{max}} = 2\pi/k_{\text{max}}$ is the wavelength of the unstable mode with maximum imaginary frequency $\max[\text{Im}(\omega_k)]$ [19,30,31]. Apart from the conservation of the total mechanical momentum [Eq. (3)] instead of the canonical momentum, an analogous process is followed in the presence of current-dependent interactions (see the recent work in Ref. [30] for details). Figure 2 illustrates the decay process of an unstable plane-wave state in a finite system of size $L = 20 n_0^{-1}$, where n_0 is the constant density, in agreement with the predictions of the linear analysis; notice [Fig. 2(a), top panel] that the canonical momentum is not a conserved quantity. The decay is apparent after $t = 20 m(\kappa n_0)^{-2}/\hbar$, as reflected by the wavy density at $t = t_1$, which is consistent with the typical time scale taken for the perturbation growth as set by the maximum imaginary frequency $\max[\text{Im}(\omega_k)]^{-1} = 5.4 m(\kappa n_0)^{-2}/\hbar$; moving and interacting solitonlike density peaks are observed afterwards, as for $t = t_2, t_f$.

The emergence of solitons from the decay of a smooth density profile is usually realized under harmonic trapping in ultracold-gas experiments (see, for instance, Refs. [5,19]). In such a setting, the system is subject to a quench in the interatomic interactions, which are changed from repulsive to attractive. The plane-wave instability analysis presented before provides just an approximation for the expected unstable modes in the inhomogeneous density profile, by assuming that the maximum density of the trapped system matches the plane-wave density. The subsequent dynamics in the trap, in the absence of current-dependent interaction and once the

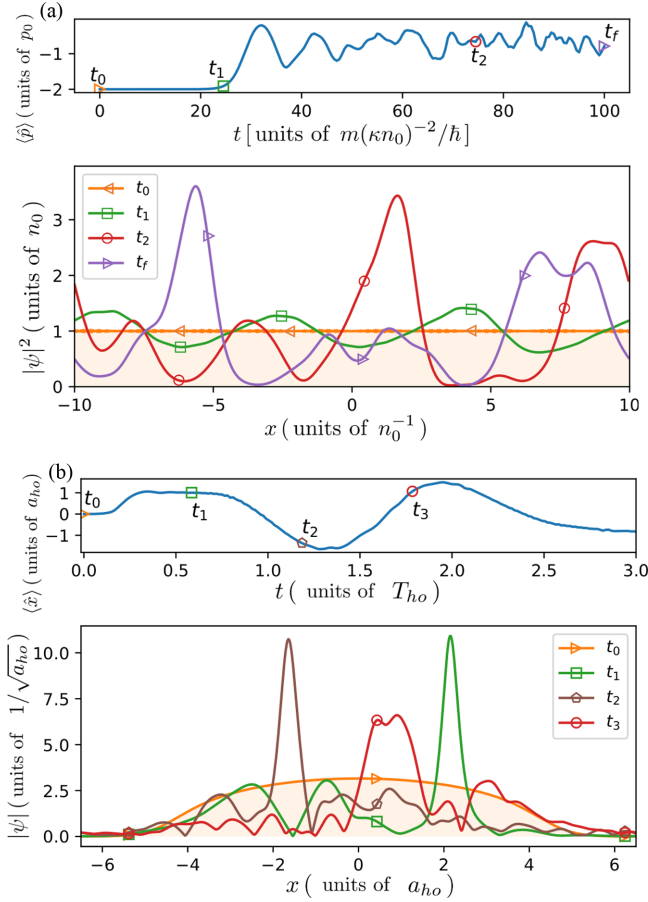


FIG. 2. (a) Decay of a plane-wave state $\psi(t_0) \equiv \psi_q = \sqrt{n_0} \exp(-i4\hbar\pi x/L)$, seeded with a random perturbation, in a finite domain of length $L = 20n_0^{-1}$ with periodic boundary conditions. The interactions are set by $g_{1D} = 0$ and $\kappa = 1$. The expectation value of the canonical momentum $\langle \hat{p} \rangle$, in units of $p_0 = \hbar n_0$, as a function of time (top panel) and snapshots of the density profile at selected times (bottom panel) are shown. (b) Decay in a harmonic trap after a sudden change in the interatomic interactions from repulsive at $t = t_0$, with $g_{1D} = 1\hbar\omega_{ho}a_{ho}$ and $\kappa = 0$, to attractive for $t > t_0$, with $g_{1D} = -0.2\hbar\omega_{ho}a_{ho}$ and $\kappa = 0.1$. The top panel shows the evolution of the center of mass, where time has units of $T_{ho} = 2\pi/\omega_{ho}$. The initial wave function $\psi(t_0)$ corresponds to the system ground state when the interactions are repulsive.

solitons have emerged, follows harmonic cycles of compression and expansion of the whole atomic cloud. As we show in Fig. 2(b), the situation is clearly different for $\kappa \neq 0$, since the Kohn theorem is not fulfilled [26], and then the system dynamics does not show harmonic oscillations.

B. Stationary bright solitons

Chiral bright solitons have been studied from the introduction of the theory of a density-dependent gauge [21,32], their dynamics [29] and stability [28] have been analyzed, and, very recently, they have been realized in translational-invariant settings [20]. In this section we briefly review their differences with respect to regular bright solitons and report on their expected features in harmonic traps, where we introduce simple approximations for static states with a usual ansatz [15].

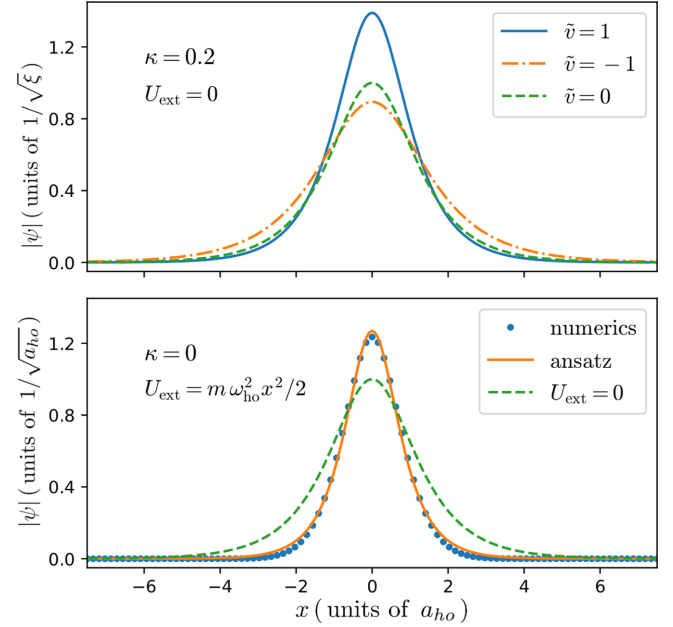


FIG. 3. Profile of bright solitons with varying velocity, parametrized by $\tilde{v} = mv\xi/\hbar$, in the presence (top panel) and absence (bottom panel) of current-dependent interactions for fixed number of particles $N = 2 \times \hbar\omega_{ho}a_{ho}/|g_{1D}|$ and contact interaction $g_{1D} < 0$. In the latter case, the comparison is made for static solitons in the presence and absence of a harmonic trap by setting $a_{ho}/\xi = 1$, where $\xi = 2\hbar^2/(m|g_{1D}|N)$ is the soliton width found in the absence of trap $U_{ext} = 0$; see main text for the ansatz description.

In the absence of both axial potential and current-dependent interaction, that is, $U_{ext} = 0$ and $\kappa = 0$, Eq. (1) admits moving-bright-soliton solutions

$$\psi = \sqrt{\frac{N}{2\xi}} \operatorname{sech}\left(\frac{x-vt}{\xi}\right) e^{i[mvx - (\mu + mv^2/2)t]/\hbar}, \quad (12)$$

where N is the number of particles, $\xi = 2\hbar^2/(m|g_{1D}|N)$ is the soliton width, and $\mu = -\hbar^2/(2m\xi^2) = -mg_{1D}^2N^2/8\hbar^3$. Note that the soliton amplitude $A = \sqrt{N/2\xi} \propto \sqrt{|g_{1D}|}N$ is directly proportional to the number of particles. Due to the U(1) symmetry of the system, a global, constant phase θ_0 can be added to the soliton phase without affecting observable features such as energy or current. For $\kappa = 0$ the system is Galilean invariant; so the soliton density profile is independent of the soliton velocity v .

When $\kappa \neq 0$, the bright soliton state equation (12) is still a steady wave solution to Eq. (1) whenever $v < v_g$; however, it acquires chiral properties [21]. Due to the current-dependent interaction, the soliton width varies with the velocity as $\xi(N) \rightarrow \xi(N, v) = 2\hbar^2/(m|g_{1D}|N)$, that is, $\xi(N, v)/\xi(N) = |g_{1D}/g_v| = (1 - v/v_g)^{-1}$. From Eq. (4), the soliton energy is $E_s = mg_v^2N^3(1 - |g_{1D}/g_v|)/(24\hbar^2) + Nm v^2/2$. Beyond a velocity threshold $v > v_g$ the bright soliton equation (12) is no longer a solution to the GP equation (1). When the stationary soliton exists, it is dynamically stable [28]. The top panel of Fig. 3 illustrates the different soliton profiles for varying velocity at fixed particle number and contact interaction; for

$v = 0$ the amplitude matches the profile of a regular soliton (with $\kappa = 0$).

Harmonic confinement

Due to its experimental relevance in ultracold gases, we consider also bright soliton states in the presence of harmonic trapping $U_{\text{ext}} = m\omega_{\text{ho}}^2 x^2/2$. In this case, a variational approach provides a good approximation to the exact solutions; see, for instance, Ref. [15]. We use the ansatz (in full units) $\psi(x) = \sqrt{N/2\xi} \text{sech}(x/\xi)$, with the width $\xi(N, \omega_{\text{ho}})$ as the variational parameter for the stationary solution. The minimization of the energy functional, as defined in Eq. (4), $E = \int dx [\hbar^2 |\partial_x \psi|^2 / 2m + m\omega_{\text{ho}}^2 x^2 |\psi|^2 / 2 + g_{1D} |\psi|^4 / 2]$, produces a quartic polynomial in ξ with a single parameter a_{ho}/ξ , where $a_{\text{ho}} = \sqrt{\hbar/m\omega_{\text{ho}}}$ is the trap characteristic length and $\xi = 2\hbar^2/(m|g_{1D}|N)$ is the soliton width found in the absence of the trap. We approximate the solution to the quartic polynomial up to second order in a_{ho}/ξ by $\xi \approx \sqrt{2/\pi} [1 - 2a_{\text{ho}}/(9\xi)] a_{\text{ho}}$ for $a_{\text{ho}}/\xi \in [0, \pi^2/4]$, and $\xi \approx \xi$ otherwise. For a fixed number of particles, the soliton width is always narrower, $\xi/\xi < 1$, in the trapped system, and the chemical potential becomes

$$\mu \approx -\frac{\hbar^2}{2m\xi^2} \left(5 - 2\frac{\xi}{\xi} \right) \frac{\xi}{3\xi}. \quad (13)$$

The bottom panel of Fig. 3 depicts these features; as can be seen, the analytical ansatz (solid line) provides a good approximation to the exact numerical result (dots); the free soliton (dashed line) is shown for comparison. When both $g_{1D} \neq 0$ and $\kappa \neq 0$, the above ansatz is still a good estimate of the ground state, and it provides a good approximation to the balance between kinetic, potential, and interaction energy. In the particular case of current-dependent interaction without contact interaction, $g_{1D} = 0$, the ground state reduces to that of the linear harmonic oscillator. However, differently from the case of just contact attractive interaction, as we will show in Sec. III D 3, when the ground state is forced to move in the trap it changes its density profile according to the effective interaction g_v determined by the velocity of the motion.

III. BRIGHT SOLITON COLLISIONS

The interaction between regular solitons has been explained, by means of the exact two-soliton solutions to the nonlinear Schrödinger equation, as a nonlinear-wave interference process during which Josephson tunneling of particles can take place [16,17]. In what follows, we elaborate on the same idea, without resorting to the exact, complicated analytical solutions, by using simple physical arguments in the analysis of chiral-soliton collisions (in the spirit of Ref. [33] on optical solitons). The soliton amplitude interference enters the dynamics through the mean-field, contact-interaction term in GP equation (1). As we will show, in regular solitons, the time evolution of noninteracting, interfering solitons captures the characteristic time and length scales of the nonlinear time evolution, and so it does when the current-density interaction is low in chiral solitons. Analogously, the current-density interaction introduces additional interference terms in the two-chiral-soliton dynamics, associated with the coupling

of amplitude and momentum of different solitons. We analyze both sources of interference, amplitude-amplitude and amplitude-momentum couplings, within the regime of non-interacting solitons, and show their relevance in the nonlinear dynamics of chiral solitons.

Our analysis starts with the superposition of two approaching, initially nonoverlapping solitons that solve Eq. (1) with particle numbers N_1 and N_2 , and relative global phase $\Theta = \theta_1 - \theta_2$:

$$\psi(x, t = 0) = \psi_{A_1, v_1, \Theta}(x + x_0) + \psi_{A_2, v_2, 0}(x - x_0), \quad (14)$$

where $d_0 = 2x_0$ is the initial intersoliton distance. To describe the dynamics, we will make use of average-soliton units (see Appendix A for details), which we will denote by barred symbols; so the length unit $\bar{\xi} = 2\hbar^2/(m|g_{1D}| + \hbar\kappa\bar{v}|N)$ is based on the average number of particles $\bar{N} = (N_1 + N_2)/2$ and average velocity $\bar{v} = (v_1 + v_2)/2$, and the time unit becomes $\bar{\omega}^{-1} = m\bar{\xi}^2/\hbar$.

A. Amplitude-amplitude interference

Although the solitons are nonlinear waves, a qualitative picture of the soliton interactions can be obtained from the usual superposition of linear waves. Due to the coherent properties of the underlying Bose-Einstein condensate, the nonoverlapping solitons of Eq. (14), separated by the distance $d = 2(x_0 - vt)$, give rise to a neat amplitude interference pattern in momentum space of period [34]

$$k_d = \frac{\pi}{x_0 - vt}, \quad (15)$$

where we assumed equal relative-velocity modulus $|v_1 - \bar{v}| = |v_2 - \bar{v}| = v$. Notice that this period increases as the solitons approach each other, and (in this approximation) it diverges, resulting in no overlapping in momentum space, at the classical collision time $t = x_0/v$.

We focus on the spatial interference as the solitons move. Before they are close enough to have a significant overlapping, the spatial interference of the solitons, $\psi_{A_1, v_1, \Theta}(t) \equiv \psi_1$ and $\psi_{A_2, v_2, 0}(t) \equiv \psi_2$, is approximated by

$$I(x, t) = |\psi|^2 - |\psi_1|^2 - |\psi_2|^2 \approx 2|\psi_1||\psi_2| \cos[k_{\text{dB}}(x - \bar{v}t) - 2v\bar{\omega}t + \Theta], \quad (16)$$

where $\psi = \psi_1 + \psi_2$, $v = (\mu_1 - \mu_2)/(2\hbar\bar{\omega})$, and $k_{\text{dB}} = 2m(v_1 - v_2)/\hbar$ is the de Broglie wave number corresponding to the de Broglie wavelength $\lambda_{\text{dB}} = 2\pi/|k_{\text{dB}}| = \pi\hbar/(mv)$. The interference manifests as an oscillatory process, $I = F \cos\phi$, characterized by an envelope wave $F(x, t) = 2|\psi_1||\psi_2|$ times a carrier wave $\cos[\phi(x, t)]$, whose phase can be recast as

$$\phi = k_{\text{dB}}\bar{\xi} \left(\frac{x - \bar{v}t}{\bar{\xi}} - \frac{v}{V}\bar{\omega}t \right) + \Theta, \quad (17)$$

where we have introduced the nondimensional parameter $V = v m\bar{\xi}/\hbar = k_{\text{dB}}\bar{\xi}/2$, which measures the relative velocity in intrinsic units $\hbar/(m\bar{\xi})$. From Eqs. (16) and (17) one can see that when the solitons have equal frequencies $\mu_1/\hbar = \mu_2/\hbar$, that is, $v = 0$, an interference pattern arises, and it is static in the moving frame with coordinates $x' = x - \bar{v}t$, as given by $I = F \cos(k_{\text{dB}}x' + \Theta)$. The pattern is observable, roughly, if

$k_{\text{dB}}\bar{\xi} > 1$; otherwise, for $k_{\text{dB}}\bar{\xi} < 1$ one would observe a net (single fringe) constructive or destructive interference according to the relative phase Θ . Overall, the relative phase just shifts, both in momentum space and in physical space, the positions of interference fringes. On the other hand, if the relative velocity vanishes, $v = 0$, one expects a time-periodic pattern (as is the case in bound soliton states) oscillating with a frequency $2v\bar{\omega}$. Far from these limit cases the interference evolves into an intermediate dynamical regime according to the ratio $|v/V|$ between the two dynamical parameters v and V .

In regard to the interference amplitude, keeping the assumption of small soliton overlapping, it can be approximated by $F(x, t) = 2A_1A_2 \operatorname{sech} \varphi_1 \operatorname{sech} \varphi_2$, where $\varphi_1 = (x + x_0 - v_1t)/\xi_1$ and $\varphi_2 = (x - x_0 - v_2t)/\xi_2$. By making use of the identities between hyperbolic functions,

$$F(x, t) = \frac{4A_1A_2}{\cosh(\varphi_1 + \varphi_2) + \cosh(\varphi_1 - \varphi_2)}, \quad (18)$$

where

$$\varphi_1 \pm \varphi_2 = \frac{\xi_2 \pm \xi_1}{\xi_1 \xi_2}(x - \bar{v}t) + \frac{\xi_2 \mp \xi_1}{\xi_1 \xi_2}(x_0 - vt). \quad (19)$$

In the absence of current-dependent interactions, $(\xi_2 + \xi_1)/(\xi_1 \xi_2) = 2/\bar{\xi}$, $(\xi_2 - \xi_1)/(\xi_1 \xi_2) = -2\alpha/\bar{\xi}$, and $A_1A_2 = \bar{A}^2(1 - \alpha^2)$, where $\alpha = (N_1 - N_2)/(2\bar{N})$ is the differential number of particles and $\bar{A} = [\bar{N}/(2\bar{\xi})]^{1/2}$ is the average soliton amplitude. The spatial modulation of the amplitude interference acts in the equation of motion as a lattice potential with time-varying depth and spatial period determined by the linear superposition of the solitons; as a consequence, it induces a corresponding modulation in the system state during its nonlinear evolution. In this way, the interaction between solitons emerging from the attractive interparticle interactions can be understood as an interference process, where attractive forces reflect constructive interference and repulsive forces reflect destructive interference. Analysis of the exact two-soliton solutions in regular solitons reveals that this is in fact the case [16,17].

B. Current-density-mediated interference

An additional source of interference is associated with the current-density interaction $\hbar\kappa J = \hbar\kappa \operatorname{Re}(\psi^* \hat{p} \psi)/m$. It involves the coupling of the amplitude and momentum of different solitons, which we will write as $\hbar^2\kappa/(m\bar{\xi})I_\kappa(x, t)$, where $I_\kappa = (\bar{\xi}/\hbar)[\operatorname{Re}(\psi^* \hat{p} \psi) - \operatorname{Re}(\psi_1^* \hat{p} \psi_1) - \operatorname{Re}(\psi_2^* \hat{p} \psi_2)]$. When there is no significant soliton overlapping, at the same order of approximation as Eq. (16), it becomes

$$I_\kappa \approx (\bar{\xi}/\hbar)[\operatorname{Re}(\psi_1^* \hat{p} \psi_2) + \operatorname{Re}(\psi_2^* \hat{p} \psi_1)] \\ = 2|\psi_1||\psi_2|[\bar{V} \cos \phi + W(x, t) \sin \phi]. \quad (20)$$

Here, $\bar{V} = \bar{v}m\bar{\xi}/\hbar$ is the non-dimensional average velocity, and $W(x, t) = \bar{\xi}[1/(2\xi_2)\tanh \varphi_2 - 1/(2\xi_1)\tanh \varphi_1]$. The cosine term in Eq. (20) keeps the same functional form as the amplitude interference [Eq. (16)], times the average velocity \bar{V} , whereas the sine term, in phase quadrature with respect to the amplitude interference, presents a space-time-varying amplitude W that depends on the relative velocity.

For well-resolved solitons, the latter quantity can be approximated before the collision by $W_0 \approx -(\xi_1 + \xi_2)\bar{\xi}/(2\xi_1 \xi_2) = -(1 - \alpha\kappa\bar{N}V/2)$ for the space between solitons, and $W_0 \approx (\xi_1 - \xi_2)\bar{\xi}/(2\xi_1 \xi_2) = (\alpha - \kappa\bar{N}V/2)$ otherwise. After the collision time, W reverses its sign; so it experiences an overall change of $2|W_0|$ during an interval of the order of $\bar{\xi}/v$ around the collision time. This fact introduces a significant asymmetry in the time evolution of chiral solitons, and different dynamical regimes arise that depend on which, \bar{V} or W , is the dominant term. In general, the interplay of the two oscillatory components in phase quadrature gives rise to a phase shift with respect to the contact-interaction term that translates into a reduction of the soliton oscillation amplitude. In addition, the time-varying interference amplitude $W(x, t)$ introduces new time frequencies in the carrier wave that are absent in regular solitons (see Appendix B for further details). Before elaborating on the more complex dynamics of chiral solitons, and in order to get better insight, we revisit the collisions between regular solitons.

C. Collisions within the nonlinear Schrödinger equation

The theory of regular-soliton collisions, mainly based on the interpretation of the complicated, exact solutions to the nonlinear Schrödinger equation, can be found elsewhere (see, e.g., Refs. [8,16,17]). We review it here from a different perspective, based on the above linear superposition analysis that led to our equations (16)–(18), and through numerical simulations that represent distinct dynamical regimes. In addition, we report approximate expressions [see Eqs. (21) and (22) below] that reproduce the main features of the process.

In the absence of both external potential and current-dependent interaction, $U_{\text{ext}} = \kappa = 0$, the seminal work of Gordon [8] revealed the nature of forces acting between nearby solitons through exact solutions to the nonlinear Schrödinger equation. The intersoliton interaction depends on three parameters featuring the differences between solitons, namely, (α, V, Θ) . In this case, α characterizes not only the differential number of particles, but also, likewise, the relative amplitude $\Lambda = (A_1 - A_2)/(2\bar{A}) = \alpha$ and the relative frequency $v = -\alpha$.

On many occasions, a simplified analysis of soliton collisions based on just one (usually Θ) or two (usually V and Θ) of these parameters is presented, which, assuming solitons with equal amplitudes $\alpha = 0$, leads to an oversimplified conclusion: In-phase solitons, $\Theta = 0$, experience attractive forces, and opposite-phase solitons, $\Theta = \pi$, experience repulsive forces between them. However, a deeper analysis shows a far richer scenario [8,9,17,35]. The interaction forces decay exponentially with the soliton distance [8], and when the solitons are within the forces' reach, two dynamical regimes that depend on the ratio $|v/V| = \alpha/V$ can be observed (assuming in this case $\alpha \geq 0$, without loss of generality). For $\alpha/V \gg 1$ the soliton interactions involve an oscillatory dynamics characterized by two frequencies: One is directly proportional to the differential number of particles α and characterizes the oscillations of the soliton amplitudes, whereas the other frequency is directly proportional to V and characterizes the exponential decay in the amplitude of the oscillations. On the other hand, for $\alpha/V \ll 1$, wave interfer-

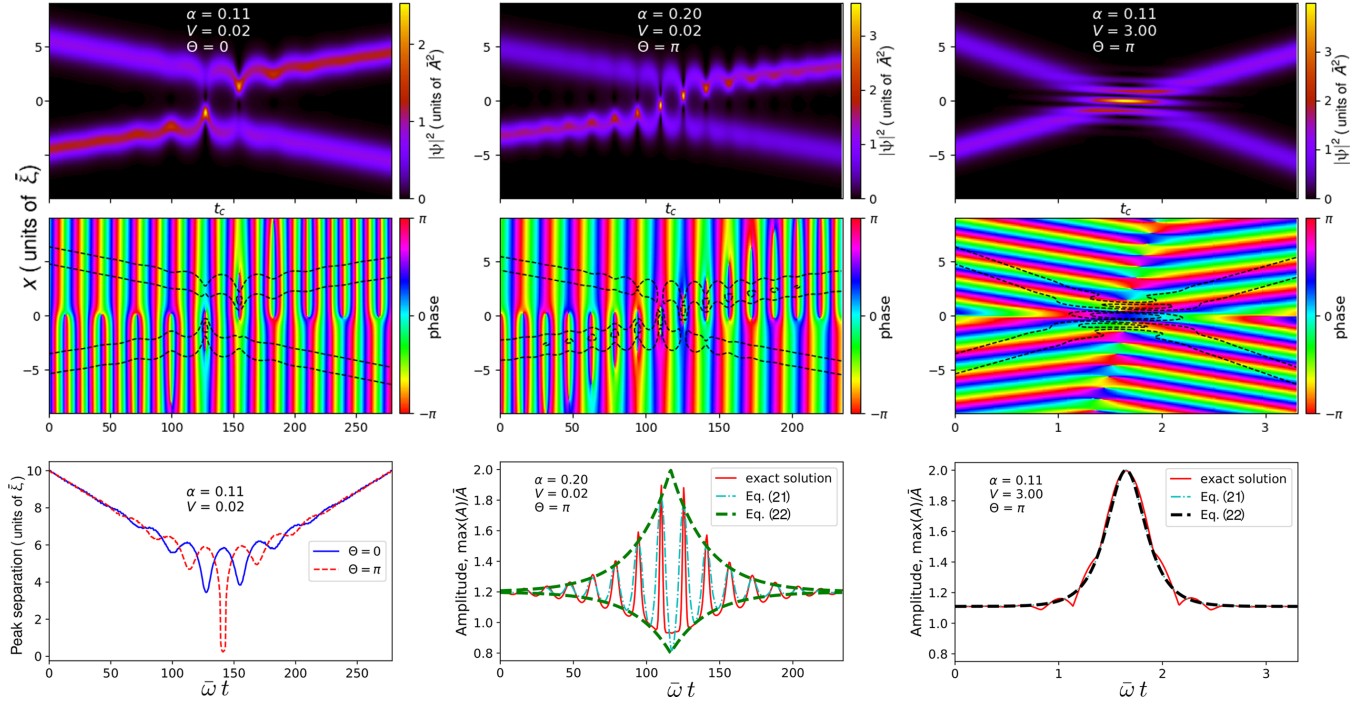


FIG. 4. Features of soliton collisions within the regular nonlinear Schrödinger equation. The time evolution of the density (top panels) and phase profiles (middle panels) is shown for varying collision parameters (with values $|v/V| = 5.5, 10,$ and 0.04 , from left to right); the dashed lines in the phase graphs represent two density isocontours. The collision time t_c is indicated on the time axis. Bottom left panel: soliton separation, as measured between density peaks. Bottom center and right panels: Time evolution of the maximum density, comparing the exact two-soliton solution with the approximate analytical expression [Eqs. (21) and (22)].

ence phenomena are dominant, and interference fringes of wavelength λ_{dB} are observed. In both collisional regimes, the soliton interactions (the proper collisions) take place mainly during the time interval $\Delta t \approx [t_c - \tau, t_c + \tau]$ for a typical time $\tau = (2V\bar{\omega})^{-1}$ around the collision time t_c (see below); before and after this time interval the solitons translate freely, conserving the properties, amplitudes and velocities, fixed by the initial conditions. The singular case with $v = 0$ gives rise to soliton bound states, whose oscillations depend on the initial intersoliton distance [8,9,17].

The collision dynamics can be summarized by the time evolution of the maximum amplitude in the system, which is well approximated by the expression

$$\max \left[\frac{|\psi(x, t)|}{\bar{A}} \right] = 1 + \alpha + f(t) \cos(2\alpha \bar{\omega}t + \Theta_0), \quad (21)$$

with an envelope function $f(t)$ given by

$$f(t) = f_0 \begin{cases} \exp(-2V\bar{\omega}|t - t_c|) & \text{if } V < \alpha \\ \text{sech}[2V\bar{\omega}(t - t_c)] & \text{if } V \geq \alpha \end{cases} \quad (22)$$

$$\text{and } f_0 = \begin{cases} 1 - \alpha & \text{if } \cos[2\alpha \bar{\omega}(t - t_c)] \geq 0 \\ 2\alpha & \text{if } \cos[2\alpha \bar{\omega}(t - t_c)] < 0, \end{cases}$$

where Θ_0 is a phase shift and $t_c = (x_0 + \Delta x)/(\bar{\xi}\bar{\omega}V)$ is the collision time obtained from the initial intersoliton distance $d_0 = 2x_0$ and the soliton-interaction displacement $2\Delta x = -\ln[(V^2 + 1)/(V^2 + \alpha^2)]\bar{\xi}/(1 - \alpha^2)$ [8]; this latter term is not captured by the estimate in Eq. (18). Figure 4 shows three examples of soliton collisions that illustrate the oscillatory

regime at low relative velocity (left and middle sets of panels) and the interference-fringe regime at high relative velocity (right panels). The time evolution of density and phase is depicted in the top and middle panels, whereas the bottom panels show the intersoliton distance (left) and the maximum amplitude (center and right), comparing the numerical solution with the analytical results given by Eqs. (21) and (22). As can be seen, these equations provide a faithful characterization of the dynamics.

Soliton collisions under harmonic confinement

Apart from the influence of the trap on single soliton amplitudes, a major influence is exerted on the dynamics of soliton collisions. Assuming that the solitons are prepared in an initial state with zero velocity at symmetric positions around the trap center $x_1 = -x_0$ and $x_2 = x_0$, the oscillator force pushes the solitons to meet at the potential minimum, where their relative velocity, proportional to the initial separation $d_0 = 2x_0$, reaches the maximum value $2v = 2\omega_{ho}x_0$. As before, this velocity v can be compared with the intrinsic velocity $\hbar/m\bar{\xi}$, as determined from the average number of particles \bar{N} (see Sec. II B) to give $V = \omega_{ho}x_0 m\bar{\xi}/\hbar = x_0 \bar{\xi}/a_{ho}^2$. Similarly to the untrapped case, the parameter $|v/V|$ determines the dynamical regime of the soliton collisions; however, an important difference arises because now $|v| \neq |\alpha|$, and the frequency difference $\nu = (\mu_1 - \mu_2)/\hbar$, as can be inferred from Eq. (13), is a nonlinear function of the differential number of particles α . Still, when $|v/V| > 1$, the system enters

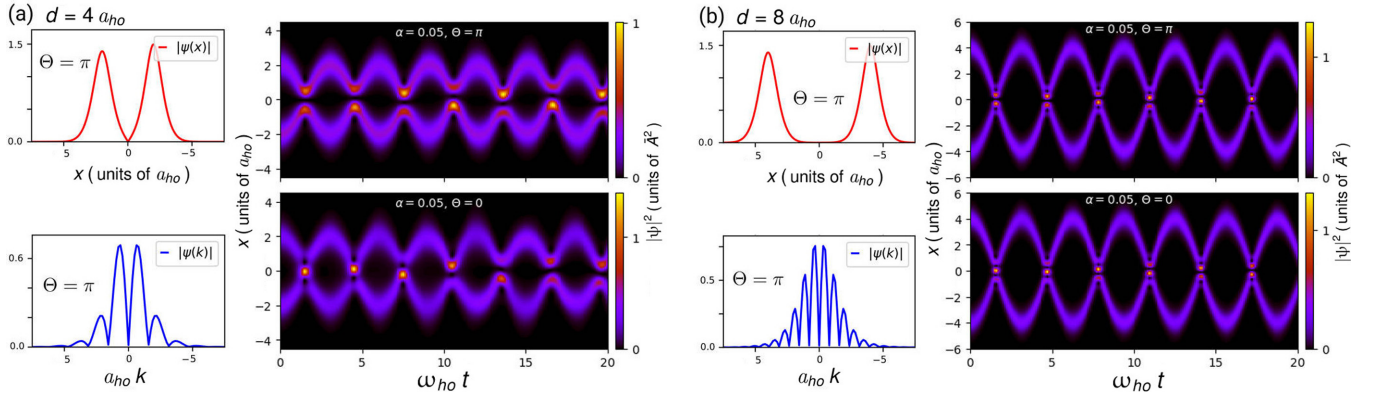


FIG. 5. Collisions between regular solitons ($\kappa = 0$) in a harmonic trap. (a) and (b) show the initial states, the amplitude profiles in physical space and momentum space, and the time evolution of the density profile for different separation and relative phase. The solitons are featured by the differential number of particles $\alpha = 0.05$, the relation between the trap and the interatomic interaction is fixed by the length ratio $a_{ho}/\xi = 1.25$, and the dynamical regimes are characterized by the ratio $|v/V| \approx 0.07$ in (a) and $|v/V| \approx 0.034$ in (b).

an oscillatory regime, whereas for $|v/V| \leq 1$ the collisions are featured by the presence of interference fringes. Figure 5 shows characteristic examples of soliton collisions in a harmonic trap. The number of particles has been fixed by $\alpha = 0.05$, while both the relative phase and the intersoliton distance (hence the eventual relative velocity) are varied. As can be seen, the repeated collisions induced by the trap force do not show identical outcomes (the motion is quasiperiodic), due to the different soliton frequency; had we kept $\alpha = 0$, we would have obtained a real periodic dynamics. As anticipated, the higher the initial separation, as in Fig. 5(b), the clearer the interference pattern.

D. Collisions subject to current-density interactions

The conservation principles in Eqs. (3) and (4), along with the additional interference terms due to the current-density interaction, rule the collision dynamics. In analogy with the amplitude interference of regular solitons, the “current interference” of chiral solitons induces an oscillatory dynamics (see Appendix B for details). Due to the velocity-dependent amplitude of the chiral solitons, the characteristic parameters of a collision change accordingly. The differential amplitude Λ becomes a function of α and the soliton velocities $v_1 = \bar{v} + v$ and $v_2 = \bar{v} - v$:

$$\Lambda = \frac{1 + \alpha}{2} \sqrt{1 - \bar{\kappa}V} - \frac{1 - \alpha}{2} \sqrt{1 + \bar{\kappa}V}, \quad (23)$$

where $\bar{\kappa} = \kappa\bar{N}/2$ provides a reference value for the current interaction strength in the system and, as before, $V = v m\xi/\hbar$. The product $\bar{\kappa}V = \hbar\kappa v/(|g_{1D} + \hbar\kappa\bar{v}|) = v/|v_g - \bar{v}|$ is a relative-velocity measure with respect to the average velocity $|v_g - \bar{v}|$, where $0 \leq v < v_g - \bar{v}$ is the condition for the solitons to exist. High relative velocities such that $v/|v_g - \bar{v}| \rightarrow 1$ indicate the high broadening and reduced amplitude of the forward moving soliton. Collisions with equal amplitudes $\Lambda = 0$, for given α and \bar{v} , correspond to the relative velocity $v_0 = |v_g - \bar{v}| 2\alpha/(1 + \alpha^2)$.

Similarly, the differential frequency can be written as a function of α and $\bar{\kappa}V$:

$$v = (\bar{\kappa}V - \alpha)(1 - \alpha\bar{\kappa}V). \quad (24)$$

Thus equal soliton frequencies $\mu_1/\hbar = \mu_2/\hbar$, which implies also equal soliton widths $\xi_1 = \xi_2$, are obtained when $\alpha = v/|v_g - \bar{v}|$. For vanishing $\bar{\kappa}V$, which is achieved not only for $\kappa = 0$ but also for zero relative velocity $V = 0$ (while \bar{v} need not vanish), the equalities $\Lambda = \alpha = -v$ of regular solitons are recovered. The ratio $v/V = (\bar{\kappa} - \alpha/V)(1 - \alpha\bar{\kappa}V)$, determining the oscillatory and interference-fringe regimes, involves now the three nondimensional parameters ($\alpha, V, \bar{\kappa}$).

Finally, the interference envelope wave $F(x, t) = 2|\psi_1||\psi_2|$, as given by Eqs. (18) and (19), is obtained with $(\xi_2 + \xi_1)/(\xi_1\xi_2) = 2(1 - \alpha\bar{\kappa}V)/\xi$, $(\xi_2 - \xi_1)/(\xi_1\xi_2) = 2(\bar{\kappa}V - \alpha)/\xi$, and $A_1A_2 = \bar{A}^2(1 - \alpha^2)\sqrt{1 - (\bar{\kappa}V)^2}$. Therefore the amplitude of the interference process is at least decreased by a factor $(1 - \bar{v}/v_g)\sqrt{1 - (\bar{\kappa}V)^2}$ with respect to regular solitons. In this regard, the current-dependent interparticle interactions reduce the soliton interactions. As we will see later, due to the phase shift between particle density and current density during the nonlinear evolution of the system, Eqs. (16) and (20), a further soliton interaction reduction can be observed in collisions at low relative velocity.

1. Collisions at low current-density interaction

The dynamical regime of low current-density interaction corresponds to $\bar{\kappa}V \ll 1$, that is, to $v \ll |v_g - \bar{v}|$. In this case, the differential amplitude equation (23) is approximated by $\Lambda \approx \alpha - \bar{\kappa}V/2$, and the differential frequency is parametrized by $v \approx \bar{\kappa}V - \alpha$. Since $v/V = \bar{\kappa} - \alpha/V$, a similar dynamics to that in the absence of current-density interactions is expected when $\bar{\kappa} \ll \alpha/V$. Figure 6 shows the outcome of chiral-soliton collisions in this latter situation. We have set a zero average velocity $\bar{v} = 0$, an interaction ratio $\hbar^2\bar{\kappa}/(mg_{1D}\xi) = 0.2$, a differential number of particles $\alpha = 0.2$, and a relative velocity determined by $V = 0.02$. As expected, the results are qualitatively similar to those in regular solitons [shown for

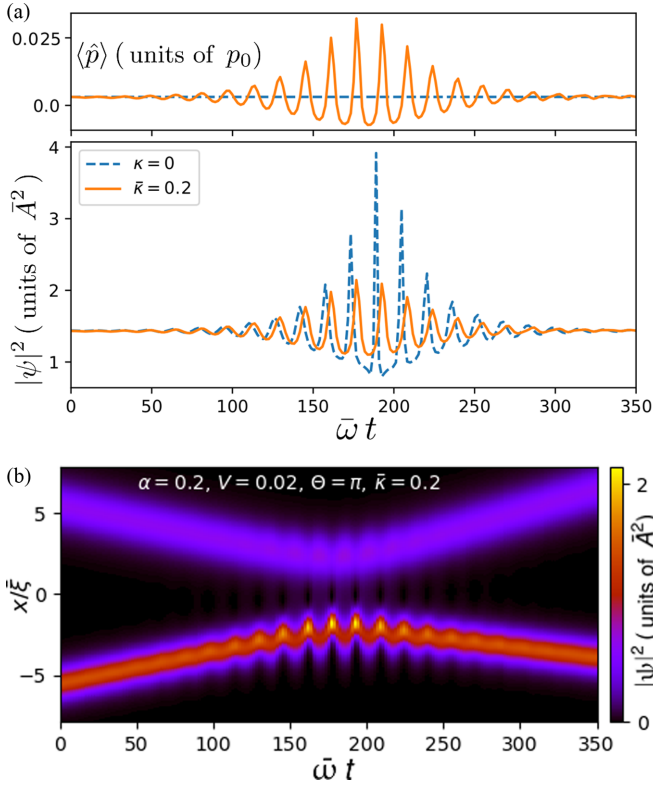


FIG. 6. Chiral-soliton collisions at low current-density interaction ($\bar{\kappa}V = 0.004$) characterized by the nondimensional parameters $\hbar^2 \bar{\kappa} / (mg_{1D} \bar{\xi}) = 0.2$, $\alpha = 0.2$, $V = 0.02$, and global relative phase $\Theta = \pi$. The average velocity of the solitons is zero, and the dynamical ratio $|\nu/V| \approx 10$. (a) shows the evolution of the system canonical momentum in units of $p_0 = \hbar/\bar{\xi}$ (top panel), along with the evolution of the maximum density (bottom panel); for comparison, the corresponding evolution for regular solitons is depicted with dashed lines. (b) shows the evolution of the density profile.

comparison in Fig. 6(a) by dashed lines], and the corresponding dynamical regime characterized by amplitude oscillations can be observed. As predicted, the amplitude oscillation period is practically indistinguishable from the case of regular solitons. Despite the fact that the canonical momentum is not a conserved quantity, only small variations are observed, and the system recovers the total initial canonical momentum after the collision event.

However, relevant differences with respect to regular solitons appear, like the peak density reduction (of about 50% in this case) and the emergence of partial or even total reflection during the collisions. It is worth comparing Fig. 6(b), which shows a total reflection of chiral solitons, with the middle set of panels of Fig. 4 for regular solitons. The latter solitons go through each other in a collision, and no reflection is produced. In contrast, chiral-soliton collisions involve in general both transmission and reflection processes that are regulated by the relative phase. Our results show that total reflection occurs at low relative velocity $|\nu/V| \gg 1$, whereas total transmission can be observed at high relative velocity $|\nu/V| \ll 1$. In this latter regime, as far as low current-density interaction $\bar{\kappa} \ll 1$ are kept, chiral-soliton collisions are even more similar to those of regular solitons, with no significant amplitude

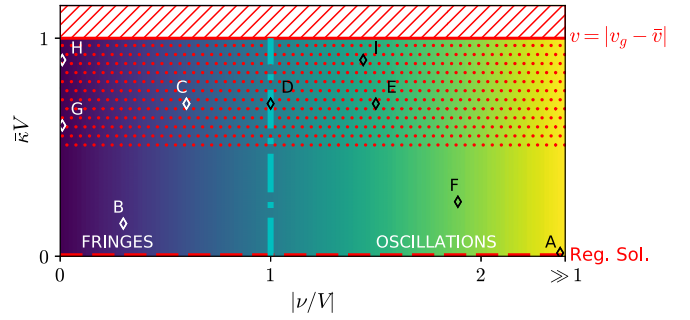


FIG. 7. Schematic phase diagram of chiral-soliton collisions as a function of the current-density interaction strength $\bar{\kappa}V$, and the ratio ν/V , which characterizes the crossover between the oscillating phase (yellow shaded region) and the regime of spatial-interference fringes (blue shaded region); the value $|\nu/V| = 1$ (dot-dashed vertical line) marks the middle point. The top red lines at $\bar{\kappa}V = 1$ indicate the relative-velocity limit, whereas the horizontal dashed line at $\bar{\kappa}V = 0$ corresponds to regular solitons. The dotted region represents the presence of nonsoliton radiation increasing with $\bar{\kappa}V$. The open symbols correspond to the discussed cases: Point A refers to the case shown in Fig. 6, point B refers to that shown in Fig. 8, points C, D, and E refer to that shown in Fig. 10, and points F, G, H, and I refer to that shown in Appendix B, Fig. 13.

reduction, and the appearance of interference fringes of wave number $k_{dB} = 2m v/\hbar$ (see Appendix B for further details).

2. General collisions

Figure 7 shows a simple phase diagram of chiral-soliton collisions as a function of the strength of the current-density interaction, as measured by $\bar{\kappa}V$, and the ratio ν/V , which parametrizes a smooth crossover, with $|\nu/V| = 1$ as the middle point (dot-dashed vertical line), between the regime dominated by soliton-amplitude oscillations (yellow shaded region) and the regime dominated by spatial-interference fringes (blue shaded region). The dotted region indicates the expected presence of nonsoliton radiation increasing with $\bar{\kappa}V$. Viewed as a scattering event of two incoming solitons, the collision produces outgoing waves that can be classified under two main sets: One set is characterized by two outgoing solitons with, in general, different velocities and amplitudes from the incoming ones; the second set includes outgoing waves that involve nonsoliton radiation along with solitons. In both sets, the initial relative phase has a strong influence on the scattering process (significantly stronger than in regular solitons), so that, for otherwise equal initial soliton parameters, different relative phases can change the outcome of the collision from one set to the other. This picture is consistent with the results of Ref. [29], where collisions between solitons with an equal number of particles, $\alpha = 0$, were addressed, and the elasticity of the collision versus the relative phase was measured through the restitution coefficient (as a ratio of incoming and outgoing kinetic energies).

A case of chiral-soliton collisions for an intermediate value of the current-density interaction $\bar{\kappa}V = \nu/\bar{v} = 0.15$ (and $g_{1D} = 0$) is shown in Fig. 8. The average soliton velocity is $\bar{V} = \bar{v} m \bar{\xi} / \hbar = 1$, and we have chosen a reference frame moving with the average velocity \bar{v} , where the solitons

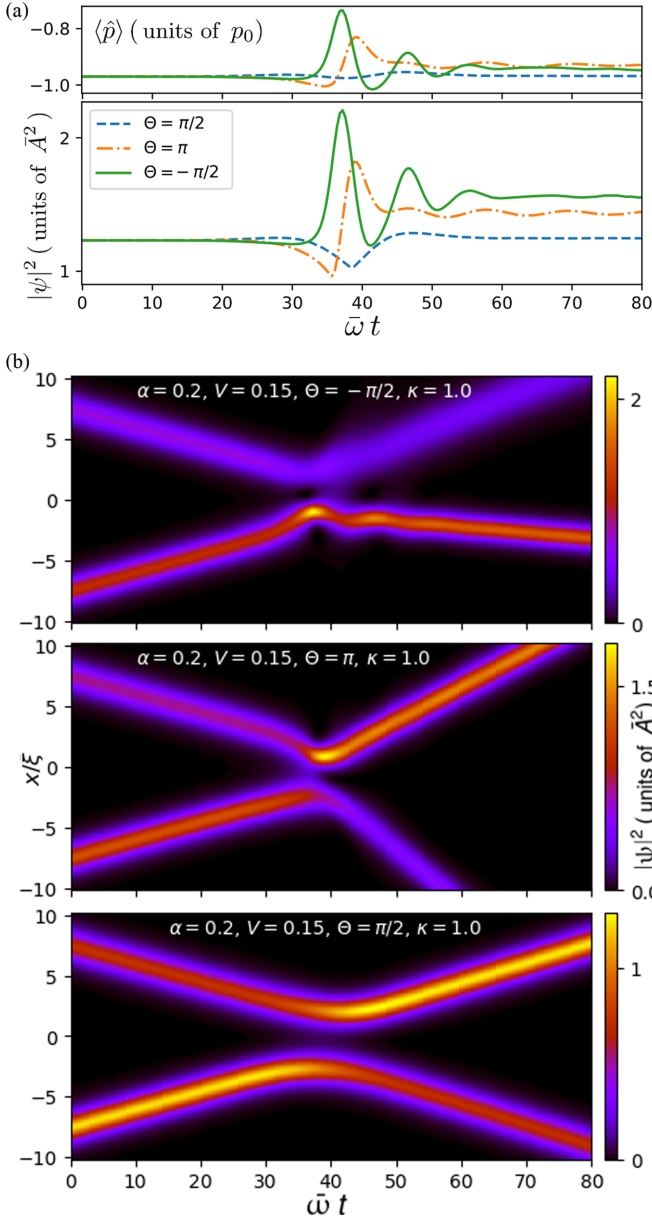


FIG. 8. Chiral-soliton collisions with no contact interactions ($g_{1D} = 0$), intermediate current-density interaction $\bar{\kappa}V = 0.15$, ratio $|v/V| = 0.3$, and varying initial relative phases Θ , as viewed in a reference frame moving with the average soliton velocity $\bar{V} = \bar{v} m \bar{\xi} / \hbar = 1$. As in Fig. 6, (a) shows the evolution of the system canonical momentum (in units of $p_0 = \hbar / \bar{\xi}$) and maximum density, whereas (b) shows the evolution of the density profile.

have equal relative-velocity modulus $|v_1 - \bar{v}| = |v_2 - \bar{v}| = v$. The differential number of particles is $\alpha = 0.2$, so that the differential amplitude and frequency become $\Lambda = 0.12$ and $\nu = -0.05$, respectively. Although the ratio $|v/V| = 1/3$ points to a nonoscillatory dynamics, the sizable influence of the relative phase Θ (shown for three particular values) gives rise to different scenarios. While at $\Theta = -\pi/2$ one can see the almost total reflection of the solitons (with a 2% variation in each soliton particle number), at $\Theta = \pi/2$ the almost total transmission (with practically conserved canonical

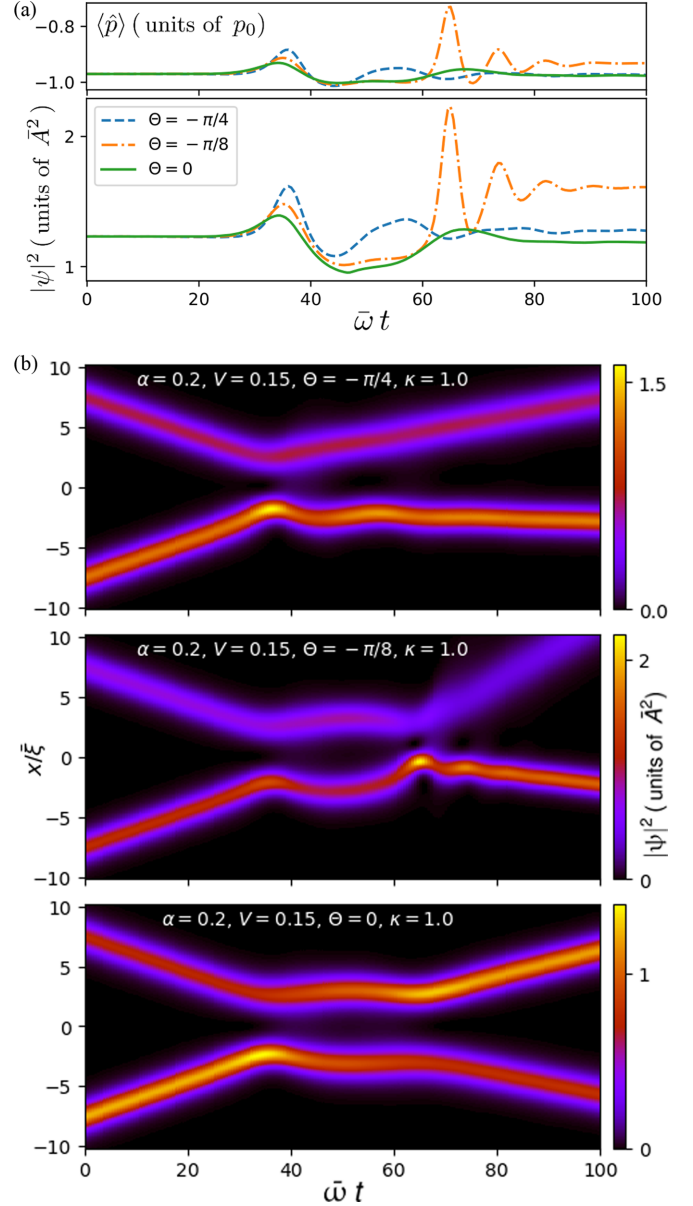


FIG. 9. (a) and (b) Same as Fig. 8, but for different values of the initial, global relative phase Θ close to the transition from predominant reflection [top panel of (b)] to predominant transmission [bottom panel of (b)] events.

momentum) is observed. In between, a highly asymmetrical outcome is produced at $\Theta = \pi$ (with an outgoing differential number of particles $\alpha = 0.4$), which, due to the conservation of the total mechanical momentum Π , Eq. (3), involves a significant change in the velocities of the outgoing solitons. The peak density achieved during the collisions is equally affected by the relative phase, with very small variation for the total transmission event. However, particular values of the relative phase close to the transition from total reflection to total transmission cause a significant variation in the duration of the collision. As can be seen in Fig. 9, one or more cycles of soliton oscillations, mediated by momentum and particle exchange, can be observed.

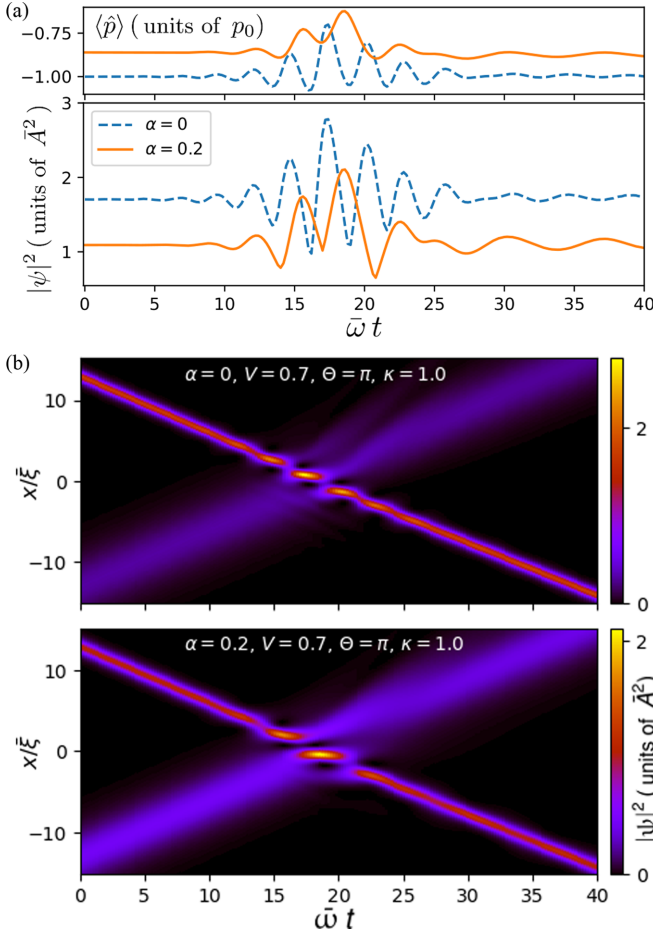


FIG. 10. (a) and (b) Same as Fig. 8, but for high current-density interaction $\bar{\kappa}V = 0.7$ and varying differential number of particles α , which translates into different dynamical ratio, differential amplitude, and frequency. They take the values $|\nu/V| = 0.6$, $\Lambda = -0.19$, and $\nu = 0.43$, for $\alpha = 0.2$, vs $|\nu/V| = 1$, $\Lambda = -0.38$, and $\nu = 0.7$, for $\alpha = 0$. That is, decreasing α moves the system horizontally to the right in the phase diagram, from point C to point D in Fig. 7; further variation (not shown) gives $|\nu/V| = 1.5$ at $\alpha = -0.2$ (point E).

High current-density interaction, as shown in Fig. 10 for $\bar{\kappa}V = 0.7$ and average soliton velocity $\bar{V} = \bar{\nu} m \bar{\xi} / \hbar = 1$, leads to the almost full transmission of the solitons through the collision, along with the appearance of interference fringes. The relative phase becomes less relevant, since it only changes the position of the maxima and minima of the interference fringes. However, the particular arrangement of the fringes is involved in the amount of nonsoliton radiation that can also be observed in this regime. The presence of radiation can be understood as related to the generation of nonlinear waves that exceed the limit speed $|\bar{\nu}|$ (in general $|v_g - \bar{\nu}|$) during the scattering event.

3. Current-density interaction and harmonic trapping

As in regular solitons, we focus on initial states with two solitons situated symmetrically around the trap center. The initial soliton separation determines the soliton speeds at collision time. Additionally, the harmonic force induces repeated collisions at twice the harmonic frequency. For our numer-

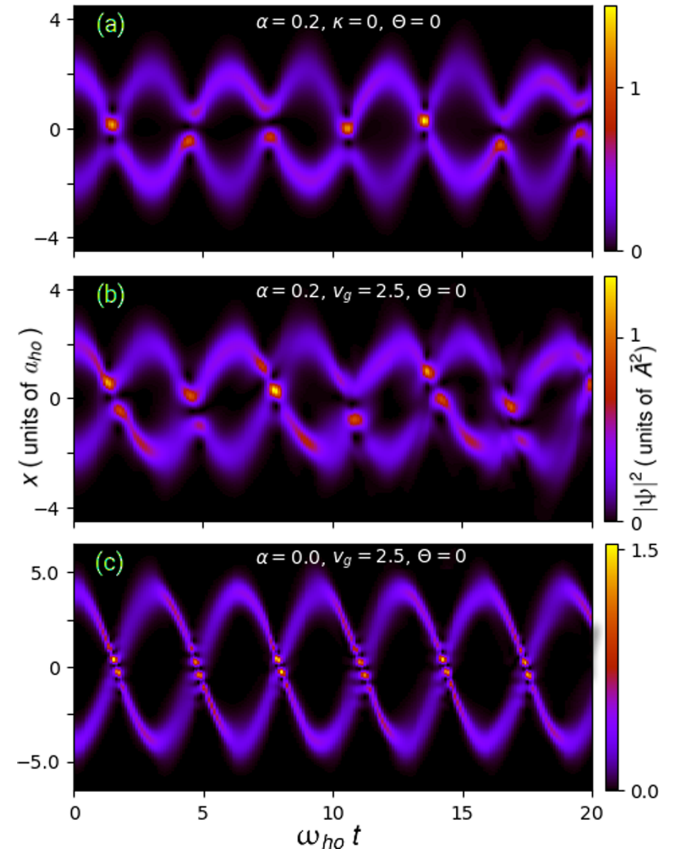


FIG. 11. Chiral-soliton collisions in a harmonic trap. (a), for regular solitons ($\kappa = 0$), is shown for comparison. In (b) and (c), the current-density interaction is characterized by the velocity $v_g = g_{1D}/(\hbar\kappa) = 2.5 \hbar/(m\bar{\xi})$.

ical simulations, the oscillator length scale and the average number of particles per soliton are chosen to give $\bar{\xi} = 0.8 a_{ho}$. Since the initial state is made of static solitons (located at the turning points of the subsequent evolution), both contact and current-dependent interactions are switched on. The strength of the latter is characterized by the velocity $v_g = g_{1D}/(\hbar\kappa)$.

Figure 11 shows several examples for varying parameters. For comparison, Fig. 11(a) depicts a case with $\kappa = 0$, differential number of particles $\alpha = 0.2$, and short soliton separation $d = 4 a_{ho}$ (that produces a small overlapping of their tails); as a consequence, the repeated collisions show different outcomes. Once again, the relative phase does not produce a qualitatively different dynamics. Figure 11(b) illustrates the system time evolution for these same parameters plus current-density interaction characterized by $v_g = 2.5 \hbar/(m\bar{\xi})$. A more complex scenario arises due to the inelastic character of the collisions, and the dynamics become more irregular at longer times. By increasing the soliton separation, as in Fig. 11(c), where $d = 8 a_{ho}$ the maximum velocity at the trap center $\omega_{ho} d / (2v_g) = 1.28$ brings the forward moving solitons into a temporarily unstable state (for $x \in [-0.875, 0.875] a_{ho}$, their effective interparticle interaction is repulsive). Nevertheless, the oscillator force is capable of balancing the dispersive effects, and the system shows repeated cycles with the characteristic interference patterns of high-velocity collisions.

IV. CONCLUSIONS

We have presented a general analysis of chiral-soliton collisions in Bose-Einstein condensates subject to current-dependent interaction. By varying the differential amplitude, the relative phase, the average velocity, and the relative velocity of the two solitons, their collision dynamics have been discussed and characterized by different dynamical regimes that give rise to oscillatory and interference phenomena. Guided by the linear superposition of the solitons, we have determined the relevant time and space scales observed in the simulations. The amplitude reduction with respect to the case of regular solitons has been revealed as a special feature in the chiral dynamics. Furthermore, in order to compare our results with feasible ultracold-gas experiments, we have investigated the influence of harmonic confinement on the emergence and the interaction of chiral solitons.

ACKNOWLEDGMENT

This work was supported by the National Natural Science Foundation of China (Grant No. 11402199), the Natural Science Foundation of Shaanxi Province (Grants No. 2022JM-004 and No. 2018JM1050), and the Education Department Foundation of Shaanxi Province (Grant No. 14JK1676).

APPENDIX A: UNITS

In the absence of external potential, the regular 1D GP equation written in nondimensional form is

$$\left\{ i \frac{\partial}{\partial \tilde{t}} + \beta \frac{1}{2} \frac{\partial^2}{\partial \tilde{x}^2} - \tilde{g}_{1D} |\tilde{\psi}|^2 \right\} \tilde{\psi}(x, t), \quad (\text{A1})$$

where $\tilde{x} = x/\ell$ and time $\tilde{t} = \omega t$ are the dimensionless coordinates, $\tilde{\psi} = \sqrt{\ell/\gamma} \psi$, with γ constant, is the nondimensional wave function, and the nondimensional parameters β and \tilde{g}_{1D} depend on the selection of units of length ℓ and time ω^{-1} :

$$\beta = \frac{\hbar^2}{m\ell^2 \hbar\omega}, \quad \tilde{g}_{1D} = \frac{g_{1D}}{\hbar\omega\ell} \gamma. \quad (\text{A2})$$

By choosing $\beta = |\tilde{g}_{1D}| = 1$, the nondimensional GP equation (A1) takes a universal form fixed by the units $\hbar\omega = m(|g_{1D}|\gamma)^2/\hbar^2$ and $\ell = \hbar^2/(m|g_{1D}|\gamma)$; the normalization becomes

$$\int d\tilde{x} |\tilde{\psi}(\tilde{x}, \tilde{t})|^2 = \frac{N}{\gamma}, \quad (\text{A3})$$

and the velocity is measured in units of $\omega\ell = |g_{1D}|\gamma/\hbar$. For the analysis of the two-soliton system we have chosen $\gamma = N/4 = \bar{N}/2$, where \bar{N} is the average number of particles per soliton. With this choice, $\int d\tilde{x} |\tilde{\psi}|^2 = 4$, and the unit of length matches the width of the average soliton $\ell = \xi = 2\hbar^2/(m|g_{1D}|\bar{N})$, that is, a soliton containing the average number of particles; the corresponding energy unit is $\hbar\omega = \hbar^2/m\xi^2 = 2\bar{\mu} \equiv \hbar\bar{\omega}$, where $\bar{\mu}/\hbar$ is the characteristic frequency of the average soliton.

Analogously, if there is only current-density interaction, the equation of motion written in nondimensional form is

$$\left\{ i \frac{\partial}{\partial \tilde{t}} + \beta \frac{1}{2} \frac{\partial^2}{\partial \tilde{x}^2} - \tilde{J} \right\} \tilde{\psi}(x, t), \quad (\text{A4})$$

where $\tilde{J} = \kappa J/\omega$ is the nondimensional current density. Since κ is dimensionless, only one parameter, β , determines the units, which, with $\beta = 1$, fulfill $\hbar\omega = \hbar^2/(m\ell^2)$. With no extra parameter introducing a fixed scale unit, Eq. (A4) is scale invariant [32]. However, the two-soliton system introduces two velocity scales, the average, \bar{v} , and the relative, $2v$, soliton velocities, with the constraint $v/|\bar{v}| < 1$. In this case, with the same normalization factor as before, $\gamma = \bar{N}/2$, we choose the units such that $\omega\ell = \hbar/(m\ell) = \kappa\gamma\bar{v}$, and then $\hbar\omega = m(\kappa\gamma\bar{v})^2$.

In the presence of both current-density, $\kappa \neq 0$, and contact, $g_{1D} \neq 0$, interaction, we rewrite the nondimensional equation (A1) with $\tilde{g} = |g_{1D} + \hbar\kappa\bar{v}|/\gamma/(\hbar\omega\ell)$, so that, by setting $\tilde{g} = \beta = 1$ and $\gamma = \bar{N}/2$ for the two-soliton system, the resulting units are $\hbar\omega = m(|g_{1D} + \hbar\kappa\bar{v}|/\hbar)^2$ and $\ell = 2\hbar^2/(m|g_{1D} + \hbar\kappa\bar{v}|\bar{N})$, in analogy with the case with only contact interactions. Thus the velocity unit is $\omega\ell = |g_{1D} + \hbar\kappa\bar{v}|\bar{N}/(2\hbar) = \kappa\gamma|v_g - \bar{v}|$, where $v_g = |g_{1D}|/(\hbar\kappa)$. Notice that $v_g > \bar{v}$ is a necessary condition for soliton existence.

APPENDIX B: GENERAL FEATURES OF COLLISIONS OF TWO CHIRAL SOLITONS

1. Energy and momentum

The lack of conservation of the canonical momentum allows for the exchange of momentum and number of particles between solitons; from Eq. (3),

$$P_t - P_0 = \frac{\hbar\kappa}{2} \int dx (|\psi_t|^4 - |\psi_0|^4), \quad (\text{B1})$$

where P_0 and P_t are the total canonical momentum of the initial ψ_0 and final ψ_t states, respectively. For the initial solitons one obtains a canonical momentum $P_0 = m(N_1 v_1 + N_2 v_2) = \bar{N}\hbar(2\bar{V} + \alpha V)/\xi$ and a momentum contribution from the gauge field $\hbar\kappa \int dx |\psi_0|^4/\bar{N} = 2\hbar\kappa\bar{N}(1 - \alpha^2)(1 + \alpha\bar{K}V)/(3\xi)$, which for the simplest case of an equal number of particles $\alpha = 0$ gives $P_0 = 2\hbar\bar{V}\bar{N}/\xi$ and $2\hbar\kappa\bar{N}/(3\xi)$, respectively.

The energy conservation equation (4) states that $E_t = E_0$, where the initial two-soliton energy is $E_0 = \sum_j N_j [mv_j^2/2 - \mu_j/3 - |g_{1D}|A_j^2/3]$, for $j = 1, 2$ and $\mu_j = -\hbar^2/(2m\xi_j^2)$. As a function of the collision parameters, the conserved energy is

$$E_t = \bar{N}\hbar\bar{\omega} \left\{ \bar{V}^2 + V^2 + \alpha\bar{V}V + \frac{2}{3}(1 + \alpha v) - \frac{2}{3} \left| \frac{g_{1D}}{g_{\bar{v}}} \right| (1 + \Lambda^2 + 2\alpha\Lambda) \right\}. \quad (\text{B2})$$

From Eq. (B1), one can see that the change in canonical momentum is accompanied by a change in the density distribution (or alternatively, in the number of particles) of the solitons. This variation is, however, limited by the conservation of energy [Eq. (B2)], which in the absence of contact interaction is just the conservation of the total kinetic energy.

2. Amplitude- and current-density-mediated interference

In general, as the schematic phase diagram of chiral-soliton collisions in Fig. 7 sketches, the picture of two dynamical regimes driven by interference, and characterized by spatial-

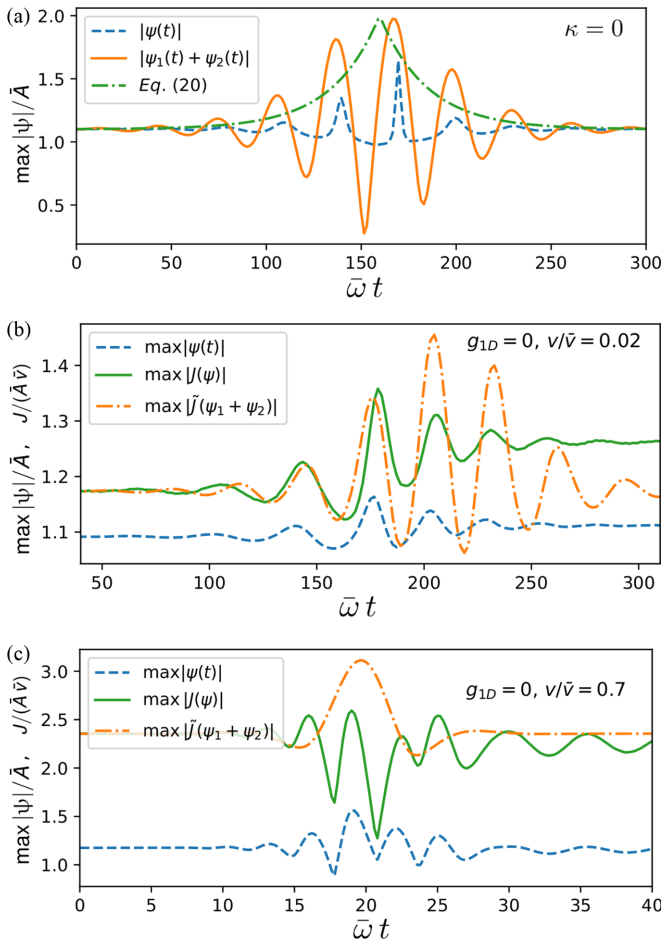


FIG. 12. (a) Nonlinear evolution of the maximum amplitude (dashed line) in a two-regular-soliton system characterized by $\alpha = 0.1$, $V = 0.02$, and $m\bar{\xi} g_{1D}/\hbar^2 = 1$. The evolution of noninteracting solitons (solid line) is shown for comparison. (b) Nonlinear evolution of the current density (solid line) and maximum amplitude (dashed line) of chiral solitons with $m\bar{\xi} \kappa \bar{v}/\hbar = 1$, no contact interaction ($g_{1D} = 0$), and otherwise the same parameters as in (a). The evolution of the current density of noninteracting solitons (dot-dashed line) is shown for comparison with a reduced and phase-shifted amplitude, \bar{J} . (c) Same as (b), but for higher relative velocity.

interference fringes and oscillatory dynamics, provides a reference framework that is complemented by the influence of the relative phase (mainly at intermediate values of the current-density interaction) and the presence of nonsolitonic radiation (increasing with the values of the current-density interaction). Close to the limits, $\bar{\kappa}V \rightarrow 0$ and $\bar{\kappa}V \rightarrow 1$, the referred spatial-interference and oscillatory regimes show more distinctive features. In order to make the picture presented in the main text more complete, in what follows, we show additional cases and details of chiral-soliton collisions.

In chiral-soliton collisions with low current-density interaction (e.g., the case depicted in Fig. 6 within the main text), the evolving noninteracting, interfering solitons, as driven by Eq. (16), captures the characteristic time and length scales of the nonlinear time evolution. This characterization is shared by regular solitons. For comparison, Fig. 12(a) depicts a simple example of regular-soliton collisions with different

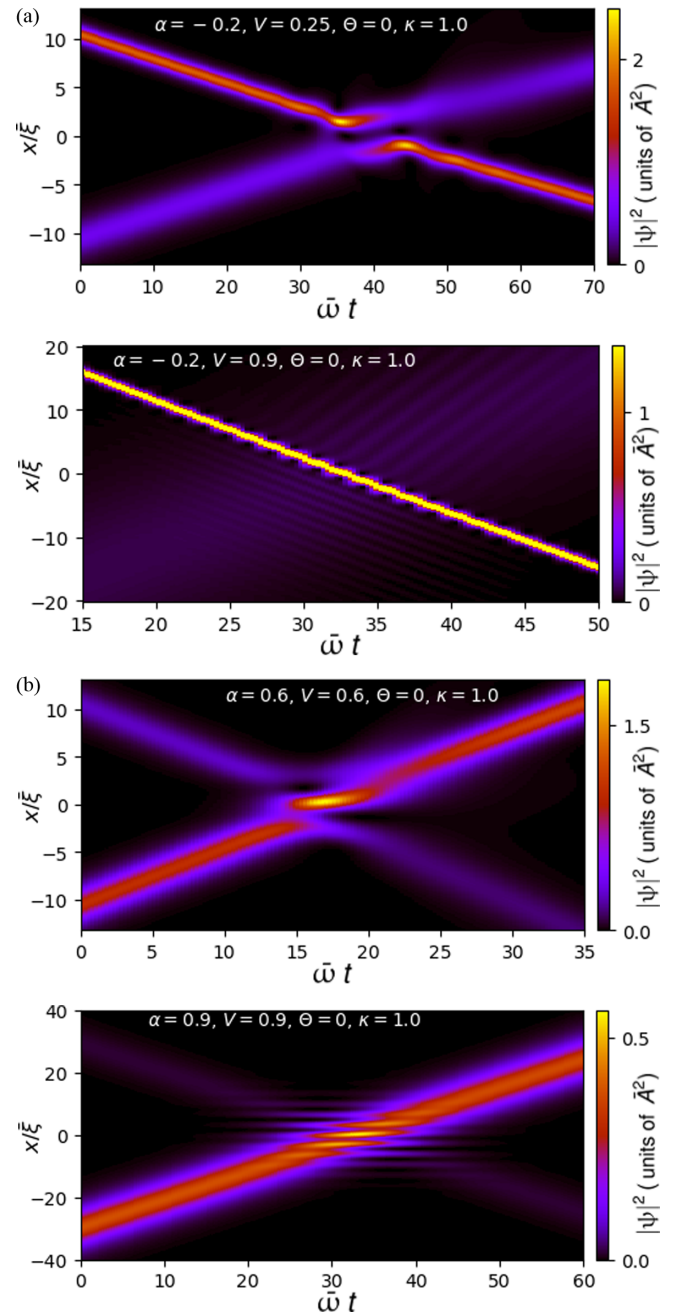


FIG. 13. (a) Chiral-soliton collisions with zero contact interaction at intermediate (top, $|\nu/V| = 1.9$) and high (bottom, $|\nu/V| = 1.4$, and reduced color map) relative velocities, both in the dynamical regime of observable soliton amplitude oscillations. (b) Same as (a), but in the dynamical regime of spatial-interference fringes with $|\nu/V| = 0$. In all cases the average velocity fulfills $m\bar{\xi} \kappa \bar{v}/\hbar = 1$.

amplitudes and low relative velocity, $\alpha/V = 5$, which shows the evolution of the system maximum amplitude. Although the amplitude oscillation predicted by the noninteracting solitons (solid line) is manifestly higher, its time period is the same, and the duration of the collision (roughly, the time during which interference is significant) is also the same.

The current-density interaction $\hbar\kappa J$ introduces additional interference terms in the two-chiral-soliton dynamics, as given

by Eq. (20), which can be recast as

$$I_\kappa \approx 2|\psi_1||\psi_2|\sqrt{\bar{V}^2 + W^2} \cos\left(\phi - \arctan\frac{W}{\bar{V}}\right), \quad (\text{B3})$$

where it is explicitly stated that the potential introduced by the current-density interaction is dephased by the time-varying angle $\arctan(W/\bar{V})$ with respect to the particle density [Eq. (16)] and scaled by the time-varying amount $(\bar{V}^2 + W^2)^{1/2}$. Figure 12(b) shows an example of chiral-soliton collisions in the absence of contact interactions, and otherwise equal parameters to those in Fig. 12(a). The average velocity is set by $m\bar{\xi}\kappa\bar{v}/\hbar = 1$, so that the differential amplitude and frequency are $\Lambda = 0.09$ and $\nu = -0.08$, respectively. The latter quantity produces a ratio $|\nu/V| = 4$ that puts the system in the oscillatory regime. The current of noninteracting solitons, depicted with a reduced and phase-shifted amplitude \bar{J} (dot-dashed line), provides a good approximation to the time frequency of the real dynamics. However, as can be seen in Fig. 12(c), at high relative velocity $v/\bar{v} = 0.7$ the linear approximation fails to provide a characteristic frequency of the collision due to a pulsating dynamics accompanied by nonsolitonic radiation. The differential amplitude and frequency are $\Lambda = -0.28$ and $\nu = 0.56$, reversing the signs of the corresponding values at low relative velocity.

Figure 13, showing cases situated in opposite limits of the schematic phase diagram of Fig. 7, illustrates how the limit of high current-density interaction $\bar{\kappa}V \rightarrow 1$ recovers a neater picture of the two dynamical regimes found in regular solitons. In Fig. 13(a), which corresponds to points F and I in the phase diagram, and where the maximum density represented in the color map of the bottom panel has been reduced by a factor of 0.4 to better show the pulsating dynamics, the ratios $|\nu/V| = 1.9$ (top panel) and $|\nu/V| = 1.4$ (bottom panel) point to an evolution characterized by soliton-amplitude oscillations. On the other hand, in Fig. 13(b), which corresponds

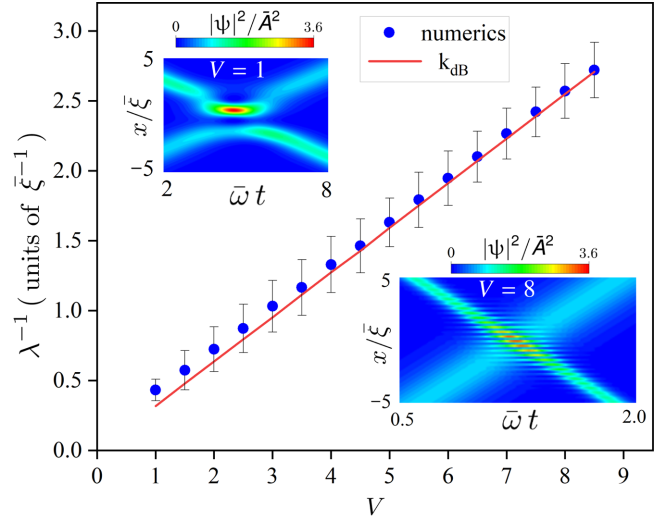


FIG. 14. Distance λ between interference fringes in counterpropagating chiral-soliton collisions as a function of the relative velocity parametrized by $V = m\bar{\xi}v/\hbar$. Both contact and current-density interactions are present, with the ratio $\hbar^2\kappa\bar{N}/(m\bar{\xi}g_{1D}) = 0.1$. The differential number of particles is $\alpha = 0.1$. The insets show the time evolution of the density profiles for two velocity values $V = 1, 8$.

to points G and H in the phase diagram, the ratio $|\nu/V| = 0$ points to the regime of spatial-interference fringes.

Interference fringes at low current-density interaction

As in regular solitons, the interference fringes that emerge from chiral-soliton collisions at low current-density interaction $\bar{\kappa}V \ll 1$ are determined by the de Broglie wave number associated with the relative velocity $k_{dB} = 2mv/\hbar$. Figure 14 shows our numerical results in this regime for chiral-soliton collisions in the presence of both contact and current-density interactions. The determination of the distance between fringes has been obtained from a Fourier analysis of the data, so that the solid circles correspond to the wave number with (nonzero, local) maximum amplitude, and the error bars indicate the width of the local maximum.

- [1] C. A. Sackett, J. M. Gerton, M. Welling, and R. G. Hulet, *Phys. Rev. Lett.* **82**, 876 (1999).
- [2] J. M. Gerton, D. Strekalov, I. Prodan, and R. G. Hulet, *Nature (London)* **408**, 692 (2000).
- [3] E. A. Donley, N. R. Claussen, S. L. Cornish, J. L. Roberts, E. A. Cornell, and C. E. Wieman, *Nature (London)* **412**, 295 (2001).
- [4] K. E. Strecker, G. B. Partridge, A. G. Truscott, and R. G. Hulet, *Nature (London)* **417**, 150 (2002).
- [5] U. Al Khawaja, H. T. C. Stoof, R. G. Hulet, K. E. Strecker, and G. B. Partridge, *Phys. Rev. Lett.* **89**, 200404 (2002).
- [6] S. L. Cornish, S. T. Thompson, and C. E. Wieman, *Phys. Rev. Lett.* **96**, 170401 (2006).
- [7] J. H. V. Nguyen, P. Dyke, D. Luo, B. A. Malomed, and R. G. Hulet, *Nat. Phys.* **10**, 918 (2014).
- [8] J. P. Gordon, *Opt. Lett.* **8**, 596 (1983).
- [9] C. Desem and P. Chu, *IEE Proc.-J: Optoelectron.* **134**, 145 (1987).
- [10] L. Salasnich, A. Parola, and L. Reatto, *Phys. Rev. Lett.* **91**, 080405 (2003).
- [11] V. Y. F. Leung, A. G. Truscott, and K. G. H. Baldwin, *Phys. Rev. A* **66**, 061602(R) (2002).
- [12] L. D. Carr and J. Brand, *Phys. Rev. Lett.* **92**, 040401 (2004).
- [13] L. D. Carr and J. Brand, *Phys. Rev. A* **70**, 033607 (2004).
- [14] B. J. Dabrowska-Wüster, S. Wüster, and M. J. Davis, *New J. Phys.* **11**, 053017 (2009).
- [15] T. Billam, A. Marchant, S. Cornish, S. Gardiner, and N. Parker, in *Spontaneous Symmetry Breaking, Self-Trapping, and Josephson Oscillations* (Springer, New York, 2012), pp. 403–455.
- [16] L.-C. Zhao, L. Ling, Z.-Y. Yang, and J. Liu, *Nonlinear Dyn.* **83**, 659 (2016).

- [17] L.-C. Zhao, L. Ling, Z.-Y. Yang, and W.-L. Yang, *Nonlinear Dyn.* **88**, 2957 (2017).
- [18] P. J. Everitt, M. A. Sooriyabandara, M. Guasoni, P. B. Wigley, C. H. Wei, G. D. McDonald, K. S. Hardman, P. Manju, J. D. Close, C. C. N. Kuhn, S. S. Szigeti, Y. S. Kivshar, and N. P. Robins, *Phys. Rev. A* **96**, 041601(R) (2017).
- [19] J. H. V. Nguyen, D. Luo, and R. G. Hulet, *Science* **356**, 422 (2017).
- [20] A. Frölian, C. S. Chisholm, E. Neri, C. R. Cabrera, R. Ramos, A. Celi, and L. Tarruell, *Nature (London)* **608**, 293 (2022).
- [21] U. Aglietti, L. Griguolo, R. Jackiw, S.-Y. Pi, and D. Seminara, *Phys. Rev. Lett.* **77**, 4406 (1996).
- [22] L. W. Clark, B. M. Anderson, L. Feng, A. Gaj, K. Levin, and C. Chin, *Phys. Rev. Lett.* **121**, 030402 (2018).
- [23] F. Görg, K. Sandholzer, J. Minguzzi, R. Desbuquois, M. Messer, and T. Esslinger, *Nat. Phys.* **15**, 1161 (2019).
- [24] K.-X. Yao, Z. Zhang, and C. Chin, *Nature (London)* **602**, 68 (2022).
- [25] M. J. Edmonds, M. Valiente, G. Juzeliūnas, L. Santos, and P. Öhberg, *Phys. Rev. Lett.* **110**, 085301 (2013).
- [26] M. J. Edmonds, M. Valiente, and P. Öhberg, *Europhys. Lett.* **110**, 36004 (2015).
- [27] R. Gao, X. Qiao, Y.-E. Ma, Y. Jian, A.-X. Zhang, and J.-K. Xue, *Phys. Lett. A* **446**, 128283 (2022).
- [28] R. J. Dingwall and P. Öhberg, *Phys. Rev. A* **99**, 023609 (2019).
- [29] R. J. Dingwall, M. J. Edmonds, J. L. Helm, B. A. Malomed, and P. Öhberg, *New J. Phys.* **20**, 043004 (2018).
- [30] I. A. Bhat, S. Sivaprakasam, and B. A. Malomed, *Phys. Rev. E* **103**, 032206 (2021).
- [31] J. Sanz, A. Frölian, C. S. Chisholm, C. R. Cabrera, and L. Tarruell, *Phys. Rev. Lett.* **128**, 013201 (2022).
- [32] R. Jackiw, *J. Nonlinear Math. Phys.* **4**, 261 (1997).
- [33] A. W. Snyder and D. J. Mitchell, *Science* **276**, 1538 (1997).
- [34] L. Pitaevskii and S. Stringari, *Phys. Rev. Lett.* **83**, 4237 (1999).
- [35] J. Satsuma and N. Yajima, *Prog. Theor. Phys. Suppl.* **55**, 284 (1974).